Hindawi
Mathematical Problems in Engineering
Volume 2024, Article ID 3713958, 17 pages
https://doi.org/10.1155/2024/3713958

*Research Article*

# Dynamics Analysis of Separation Mechanism for Rotating Projectiles at the End of Trajectory

**Lei Zhao**,[1] **Shuai Yue**,[2] **Zhong-hua Du**,[2] **Teng-fei Ma**,[3] **and Xing-xiao Li**[4]

[1]*School of Equipment Engineering, Shenyang Ligong University, Shenyang 110158, China*
[2]*School of Mechanical Engineering, Nanjing University of Science and Technology, Nanjing 210094, China*
[3]*The Fourth Military Representational Office of the Air Force Equipment Department, Shenyang 110027, China*
[4]*Liaoning Northern Huafeng Special Chemical Co. Ltd., Shenyang 113003, China*

Correspondence should be addressed to Shuai Yue; yueshuai@njust.edu.cn

Received 3 November 2023; Revised 21 February 2024; Accepted 2 March 2024; Published 30 March 2024

Academic Editor: Babak Shotorban



Spin separation technology is a key technology for realizing the detection function at the end of the rotational trajectory. It is also a necessary condition for the fuse control system to adjust its control strategy according to actual combat needs. To explore a new type of proximity fuse detection method, this article first designs a detection separation mechanism for the end of the trajectory. An interior ballistic model of the separation mechanism was then established through closed bomb tests and equivalent interior ballistic equations, and the aerodynamic parameters of the front-stage separation body at the moment of separation were obtained based on computational fluid dynamics numerical simulation. Finally, a separation dynamics model of the separation mechanism was established to analyze the motion state after the separation action of the front-stage separation body. The results demonstrate the feasibility of the proposed separation mechanism. The discrepancy between the simulation and experiment of the velocity increment for the front-stage separation body is about 1.07%. The attack angle for the front-stage separation body is below 2°, and the period with a displacement between two stage bodies greater than 3 m is around 0.365 s. This research can provide new ideas and theoretical references for the design of a similar fuse detection separation mechanism.

## 1. Introduction

The reliable completion of separation action by the spinning projectile's trajectory-end detection separation mechanism is crucial for the success of flight missions. The trajectory-end detection separation mechanism, as one of the core components of the projectile control system, utilizes target information, platform information, and environmental information to control the fuze according to a predetermined strategy [1–3]. When conducting dynamic research on separation mechanisms based on pyrotechnic separation, obtaining key geometric and physical parameters of the mechanism dynamics can be challenging. Generally, researchers simplify mathematical models and combine them with simulation software for their studies [4].

Regarding the study of dynamic separation in spinning projectiles with trajectory-end detection, literature [5] states that the combustion process of propellant in the chamber of a gun is essentially the same as that in a closed bomb before the projectile's motion. Literature [6] uses a closed bomb to investigate the combustion and gas formation of propellant under constant volume conditions and combines it with computational fluid dynamics (CFD) for modeling and simulation. The effectiveness of the model was verified through experiments. In literature [7], a separation scheme utilizing thrusters and lateral rockets as separation energy sources was designed. Dynamic models were established for the constrained separation stage and free-flight stage in a nonrotational state. Dynamic simulations of the separation process were conducted, resulting in the analysis of the movement and distribution of the missile fairing. In literature [8], the internal structure of pyrotechnic separation mechanisms was optimized. A model of a conical piston impacting a thin-walled tube damper was established, analyzing the characteristics of the damper and its relationship with the cone angle and damper performance. Literature [9] studied the influence

of different connection methods between missile bodies and engines on two-stage missile separation. Simulation results showed that the different connection methods had little impact on the separation between the missile body and engine. In literature [10], a system formula for rigid body dynamics simulation of carrier rockets (including short-period dynamics) was proposed. It included the inherent short-period dynamics of stage separation and jettisoned components. Statistical analysis of the upper-stage separation process was conducted to study the impact of design variables on the separation body.

In summary, the current research on the dynamic separation of projectiles by scholars both domestically and internationally mainly focuses on the interior ballistic characteristics of separation mechanisms, the dynamics of projectile-fairing separation, and the dynamics of projectile-engine separation. However, there are no existing studies specifically addressing the dynamic aspects of a trajectory-end detection separation mechanism for spinning projectiles. Since the carrier of the separation mechanism is a spinning stabilized projectile, the essence of the study on the dynamic separation of projectiles at the end of the trajectory in this paper is to explore the dynamic separation problem of the projectile detonator separation mechanism in a rotating state. Therefore, research on rotating separation technology becomes a necessary link to determine the feasibility of the separation mechanism. In response to the dynamic separation problem of the projectile detonator separation mechanism in a rotating state, this paper designs a detection separation mechanism for the end of the trajectory and studies its dynamic characteristics through closed bomb experiments and numerical simulation.

The organization of this paper is as follows: Section 2 introduces the structure, working principle, and parameter design and analysis of the separation mechanism. In Section 3, closed bomb tests and simulations of the separation mechanism are conducted, followed by a comparative analysis of the results and an investigation of its internal ballistic characteristics. Section 4 establishes an aerodynamic model for the preseparation body of the separation mechanism and analyzes the results of the aerodynamic simulation calculations. Section 5 focuses on studying the dynamics characteristics of flight vehicle separation, with a particular emphasis on the separation velocity, displacement difference, and variation of the attack angle of the preseparation body. Finally, Section 6 provides the research conclusions.

## 2. Separation Mechanism Structure Principle and Parameter Design

*2.1. Structure and Operating Principles of the Separation Mechanism.* The logic diagram of the separation mechanism designed in this paper is shown in Figure 1.

As shown in Figure 1, when the projectile reaches the target area, the annular ejection propellant container will be immediately ignited. The resulting high-pressure gas will propel the front-stage separation body and shear off the copper shear pin. At the same time, the wire will detach from the main body along with the front-stage separation body at a velocity, flying toward the target area. When the front-stage separation body contacts the target or an obstacle, it receives a feedback electrical signal. This feedback signal serves as the basis for the projectile's fuze control system to determine the next instruction. The model of the separation mechanism is shown in Figure 2(a), and the main dimensions are presented in Figure 2(b). The parameter descriptions can be found in Table 1.

The separation mechanism is mainly composed of detection module 1, base 2, detection module housing 3, wire 4, copper shear pin 5, annular ejection propellant container 6, and main body 7. The detection module 1 is welded to wire 4 and integrated with the detection module housing 3 through a polyurethane potting compound, forming a cohesive unit. This unit is fixed on the base 2 using threaded connections to form the front-stage separation body. The annular ejection propellant container 6 is secured in the annular groove of the main body 7 with screws. The front-stage separation body and the main body are held together by two copper shear pins 5, forming a complete separation mechanism.

*2.2. Parameter Design and Analysis of Separation Mechanism.* After the separation action of the separation mechanism, assuming the velocity of the separation mechanism body is $V_0$, and the velocity of the front-stage separation body relative to the body is $V_k$, where $v_k - v_0 = \Delta v > 0$, with $\Delta v$ representing the velocity increment of the front-stage separation body relative to the main body, The front-stage separation body, after completing the separation, can maintain a stable flight distance of $L_{\max}$ for at least $t_{\max}$. As shown in Figure 1, if the separation between the two stages fails, the projectile's fuze control system will not receive feedback signals and cannot make judgments for the next instruction.

Parameter design is a crucial aspect of the separation problem, as the scientificity of parameter design directly impacts whether the separation mechanism can successfully achieve the intended objectives [11]. Parameter design mainly includes the force design requirements and mechanism parameter design [12]. The longitudinal separation force is primarily provided by the annular ejection propellant container. Once the separation command is issued, the annular ejection propellant container immediately exerts its effect. According to the law of conservation of energy, to reliably complete the separation action, the work done by the thrust $F_a$ generated by the combustion of propellant must satisfy.

$$F_a \cdot s > \frac{1}{2} m \left(\frac{s}{t}\right)^2, \tag{1}$$

where $s$ represents the internal ballistic displacement of the front-stage separation body, $t$ represents the duration of action inside the annular ejection propellant container, and $m$ represents the mass of the front-stage separation body.

After the separation mechanism completes the separation action, the relationship between the total external force $F_s$ acting on the front-stage separation body, the flight distance $L_{\max}$, and the velocity increment $\Delta v$ relative to the main body must satisfy.

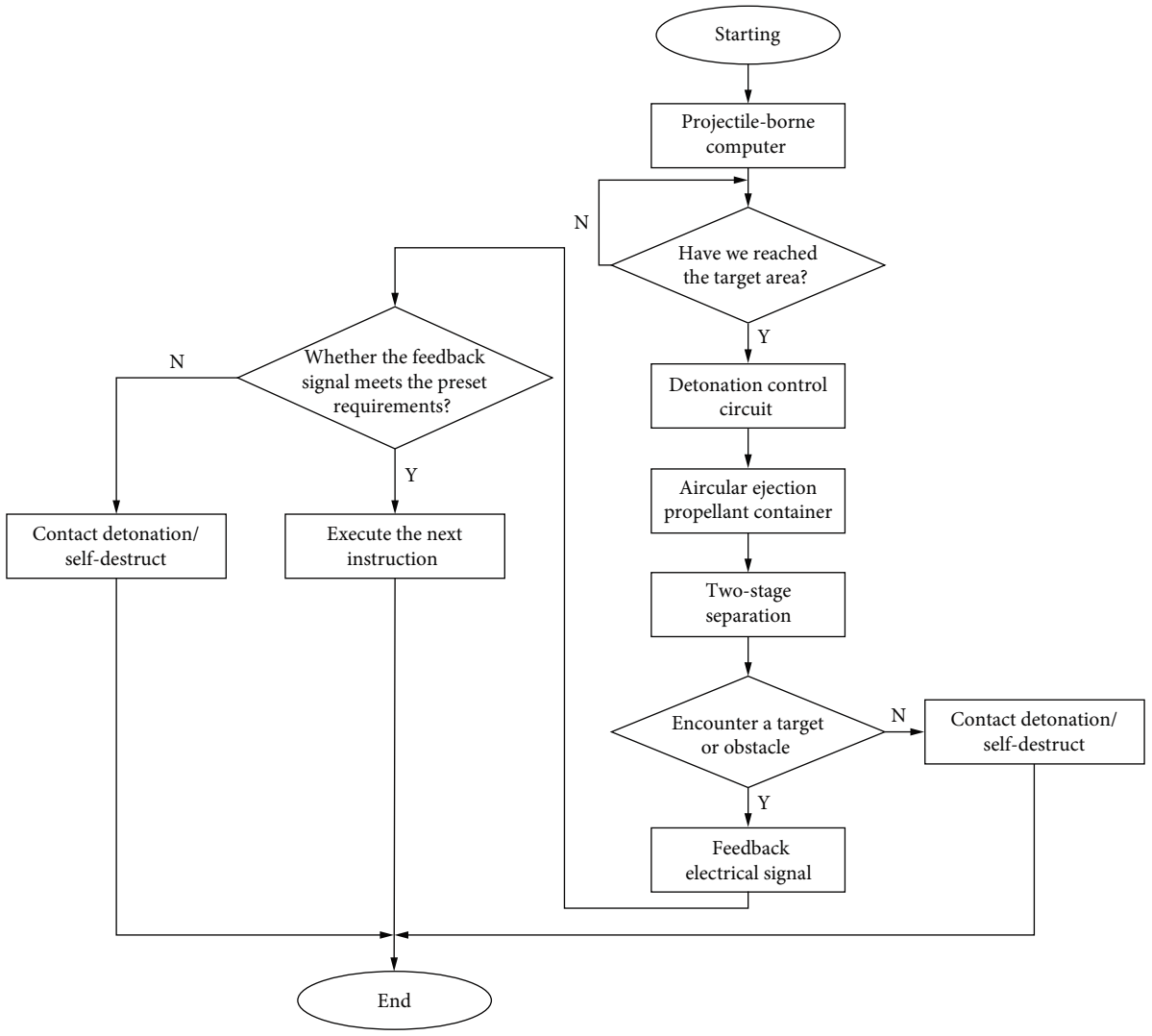


FIGURE 1: Logic diagram of the separation mechanism.

$$\begin{cases} (v_k - v_0) + \dfrac{F_s}{m} t_{\max} \geq \Delta v, \\ (v_k - v_0) t_{\max} + \dfrac{1}{2} \dfrac{F_s}{m} t_{\max}^2 \geq L_{\max}, \end{cases} \tag{2}$$

where $F_s = R + F_d + G$, where $R$ represents the total aerodynamic force, $F_d$ represents the tension in the wire, and $G$ represents gravity.

According to the actual requirements of a certain type of artillery shell fuze, the following predetermined parameter requirements are proposed for the velocity increment $\Delta v$ of the front-stage separation body, the change in attack angle $\delta$, and the displacement difference $\Delta l$ between the two stages, as shown in Table 2.

## 3. The Internal Ballistic Characteristics of the Separation Mechanism

To further investigate the internal ballistic characteristics of the separation mechanism, this section conducts closed bomb tests at different temperatures to obtain the chamber pressure $f$ and the burning rate coefficient $u_1$ of the propellant. These parameters are then used as inputs for the separation dynamic model calculation of the separation mechanism.

*3.1. The Comparative Analysis of Simulation and Experimental Results.* In this section, the combustion characteristics of the pyrotechnic product used in the separation mechanism under constant volume conditions are studied through closed bomb tests. Two important parameters, peak pressure $P_{\max}$ and peak time $T_{\max}$, are obtained from the experimental results. These parameters are then used to determine the chamber pressure $f$ and burning rate coefficient $u_1$ in the propellant burning rate equation, which is used for the internal ballistic characteristics analysis of the separation mechanism.

According to the first law of thermodynamics [13],

$$dQ = dE + pdW, \tag{3}$$

where $dQ$ represents the change in thermal energy entering the working volume, $dE$ represents the change in the internal

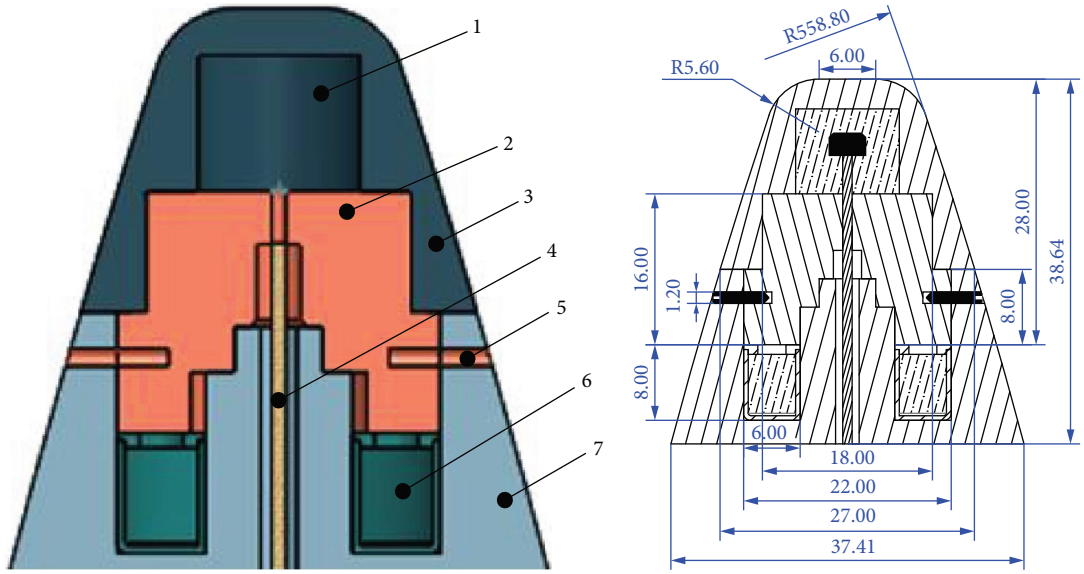


(a) (b)

Figure 2: Schematic diagram of the separation mechanism: (a) model schematic diagram; (b) main dimensions schematic diagram.

Table 1: The material for the main parts.

| Number | Part | Material | Mass (g) |
|---|---|---|---|
| 1 | Detection module | — | 50 |
| 2 | Base | Copper | |
| 3 | Detection module housing | Aluminum alloy | |
| 4 | Wire | Copper | |
| 5 | Copper shear pin | H62 brass | |
| 6 | Annular ejection propellant container | Aluminum alloy | |
| 7 | Main body | Aluminum alloy | $2.176 \times 10^4$ |

Table 2: Predetermined parameters.

| Number | Parameters | Value |
|---|---|---|
| 1 | Velocity increment $\Delta v$ (m/s) | 40–50 |
| 2 | Angle of attack variation $\delta$ (°) | ≤10 |
| 3 | Displacement difference $\Delta l$ (m) | 3–10 |

energy of the gas, and $pdW$ represents the change in work done by the gas expansion.

Under constant-volume conditions, due to the small volume of the propellant itself, the contribution of $P$dW can be neglected. Therefore, it can be assumed that all the thermal energy generated by the combustion of the propellant is converted into the internal energy of the gas. As the mass of the gas $\omega_g = \omega\psi$ continuously increases, the corresponding heat also increases.

$$Q = Q_W \omega_g \,, \tag{4}$$

where $\omega$ represents the mass of the propellant charge, $\psi$ represents the ratio of burned propellant mass, $\omega_g$ represents the mass of gas generated by propellant combustion, and $Q_w$ represents the heat of explosion of the propellant.

Under constant-volume conditions, especially for the closed bomb device, the chamber pressure can be expressed as follows:

$$p = \frac{RT_1\omega\psi}{W} = \frac{f\omega\psi}{W}, \tag{5}$$

where $f = RT_1R$ represents the gas constants, $f$ represents the chamber pressure, $T_1$ represents the explosive temperature, and $W$ represents the volume of the propellant gas.

From the above equation, it can be inferred that under constant volume conditions, the chamber pressure depends on the ratio of burned propellant mass. When the ratio of burned propellant mass is $\psi$, the equation becomes $p_\psi = p$, $W_\psi = W$ Therefore,

$$p_\psi = \frac{f\omega\psi}{W_\psi}, \tag{6}$$

where $W_\psi$ represents the free volume of the chamber.

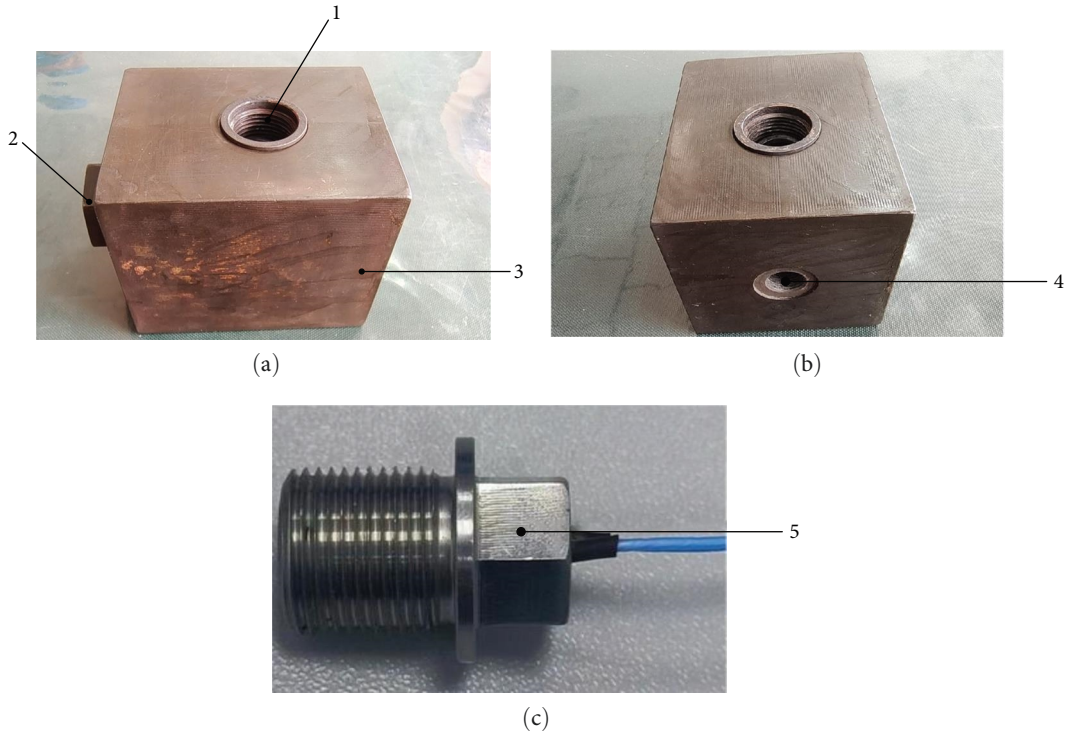


FIGURE 3: Closed bomb device. 1—Ignition mechanism interface, 2—Exhaust port, 3—Metal body, 4—Pressure sensor interface, 5—Ignition mechanism (a–c).

According to Equation (6), it can be inferred that the maximum pressure value $P_{\mathrm{mm}}$ under constant volume conditions occurs at the moment when the propellant combustion is completed. Therefore,

$$p_{\mathrm{mm}} = p_{\psi=1} = \frac{f\omega}{W_0 - \alpha\omega}, \tag{7}$$

where $W_0$ represents the initial volume of the medicine cabinet.

Introducing the concept of packing density $\Delta = \frac{\omega}{W_0}$ and substituting it into the equation above,

$$p_{\mathrm{mm}} = \frac{f\Delta}{1 - \alpha\Delta}. \tag{8}$$

To study the performance of propellant at different temperatures and avoid randomness in experiments, closed bomb tests were conducted at +70, +20, and −55°C, with three tests performed at each temperature. The closed bomb device, shown in Figures 3(a) and 3(b), consists of a pressure sensor interface 1, an exhaust port 2, a metal body 3, and an ignition mechanism interface 4. The ignition mechanism, as shown in Figure 3(c), is specifically designed to simulate real-world operating environments and is typically used to test the actual output pressure of pyrotechnic products as a basis for assessing their output capabilities.

The functioning process of the closed-bomb devices is as follows: First, the tested pyrotechnic product is assembled inside the ignition mechanism 5, creating an independent test sample, as shown in Figure 3(c). Then, the assembled test sample is screwed into the ignition mechanism interface 4 of the closed bomb device, while the pressure sensor is installed together with the pressure sensor interface 1. Finally, the ignition mechanism 5 is electrically ignited using a DC power source, causing the pyrotechnic product to burn. As a result, the pressure sensor outputs the pressure value, allowing the determination of the output pressure and its variation characteristics of the pyrotechnic product under constant chamber volume conditions.

In this experiment, the inner cavity volume of the closed bomb device was 10 ml, and the mass of the pyrotechnic composition was 200 mg.

By establishing the interior ballistics equation under constant volume conditions, we can obtain two key parameters of propellant: chamber pressure $f$ and burning rate coefficient $u_1$. The experimental and simulation results are shown in Figures 4–6, and it can be observed from the pressure curve that the simulation results are in good agreement with the experimental results. At different temperatures, the pressure curve gradually increases from zero until it reaches a stable state. Under constant-volume conditions, during the initial ignition phase, the chamber pressure increases gradually as the propellant burns. When the propellant gases fill the container, the chamber pressure will remain stable until the explosion is completed.

During the experimental process, the pressure sensor may collect some data that approaches zero as time increases during the initial combustion stage of the propellant. This can lead to a time lag between the experimental and simulated pressure curves, requiring a shift in the time axis of the

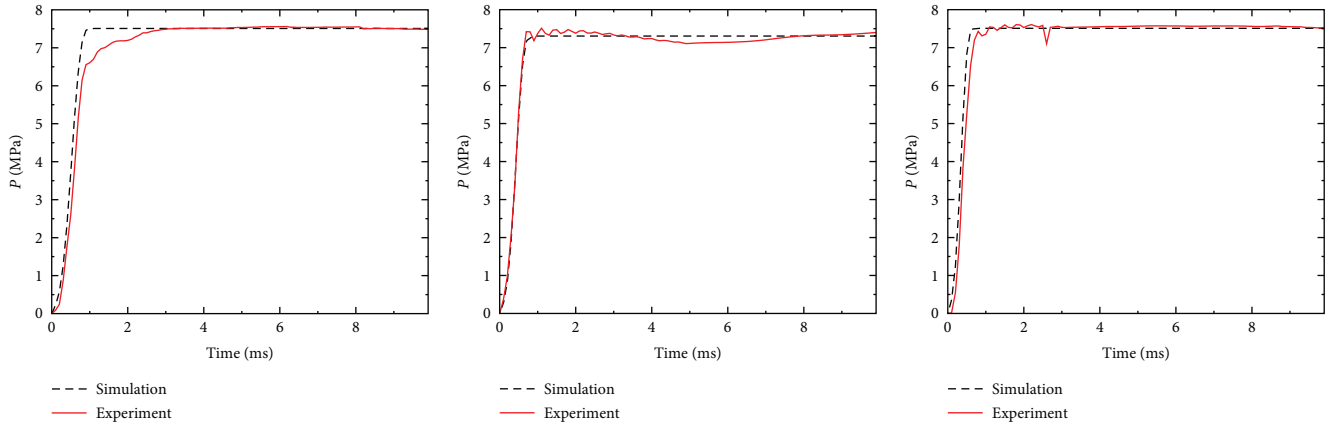


Figure 4: +70°C: (a) #1; (b) #2; (c) #3.

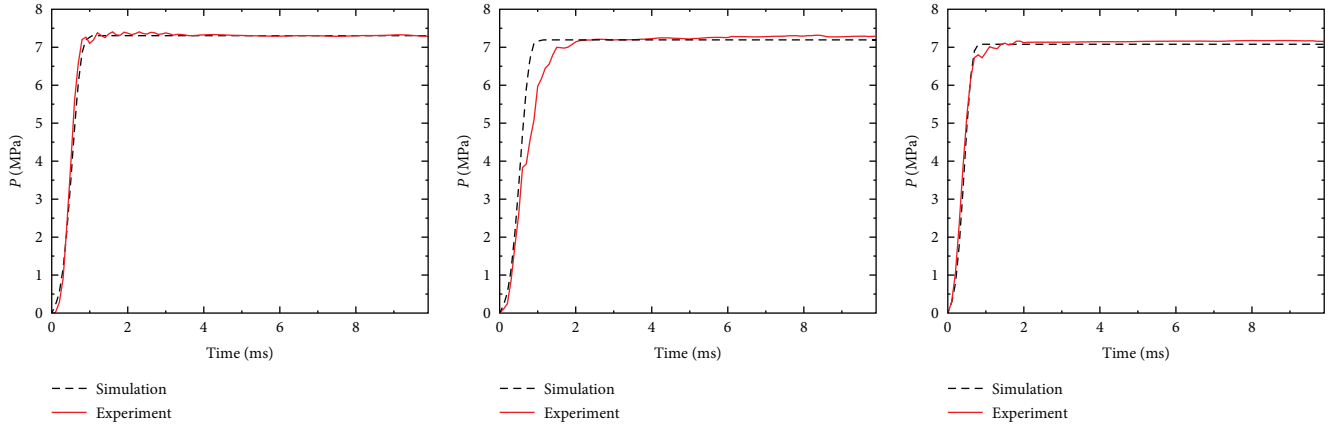


Figure 5: +20°C: (a) #1; (b) #2; (c) #3.

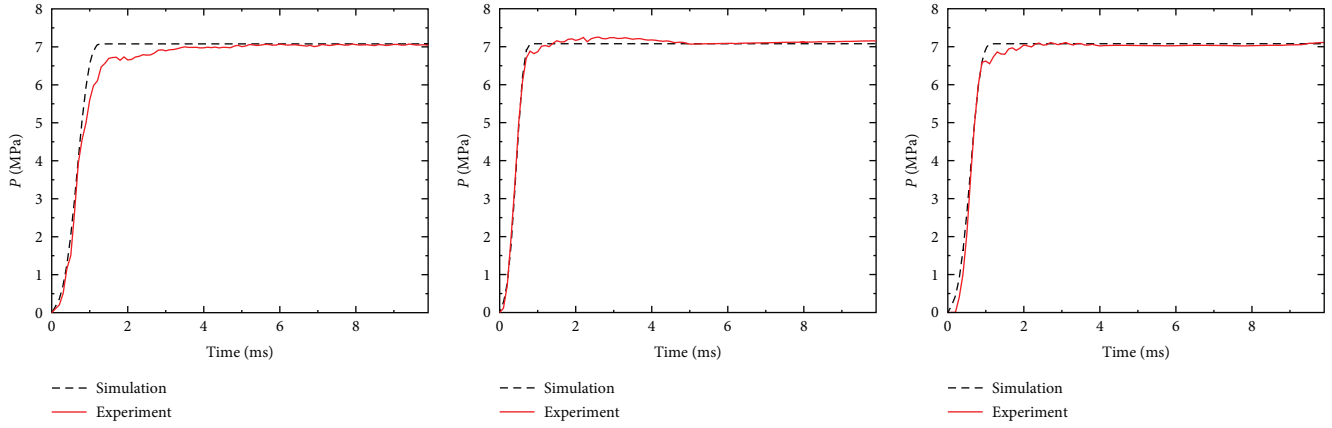


Figure 6: −55°C: (a) #1; (b) #2; (c) #3.

Table 3: Table of test and simulation of closed bomb tests.

| Temperature (±2) (°C) | Number | $P_{emax}$ (MPa) | $P_{smax}$ (MPa) | Error (%) | $u_1$ (e7·mm·(MPa/s)) | $f$ (MJ/kg) |
|---|---|---|---|---|---|---|
| +70 | 1 | 7.55 | 7.51 | 0.53 | 2.5 | 0.355 |
| | 2 | 7.51 | 7.31 | 2.70 | 2.4 | 0.348 |
| | 3 | 7.57 | 7.50 | 0.92 | 2.5 | 0.350 |
| +20 | 1 | 7.36 | 7.31 | 0.54 | 2.1 | 0.344 |
| | 2 | 7.31 | 7.19 | 1.60 | 2.0 | 0.342 |
| | 3 | 7.25 | 7.08 | 2.34 | 1.9 | 0.338 |
| −55 | 1 | 7.07 | 7.08 | 0.05 | 1.6 | 0.341 |
| | 2 | 7.20 | 7.08 | 1.67 | 1.6 | 0.331 |
| | 3 | 7.10 | 7.07 | 0.42 | 1.6 | 0.339 |

simulated pressure curve to ensure the accuracy of internal ballistic parameters. The error in the initial pressure curve in the experimental data can be ignored as it does not affect the peak pressure and peak time of propellant combustion, as shown in Figures 4(c) and 6(c).

Based on the experimental data and the solution of the constant volume interior ballistics equation, the peak pressure $P_{max}$, combustion rate coefficient $u_1$, chamber pressure $f$, and the error between the experimental and simulated results *Error* are shown in Table 3 for different temperatures. $P_{emax}$ represents the peak chamber pressure from the experiment, while $P_{smax}$ represents the peak chamber pressure calculated in the simulation. By comparing the experimental data with the simulation results, the maximum error in the simulated peak pressure is 2.7%, and the minimum error is 0.05%. This indicates that the error in the simulated results of interior ballistics under different temperatures can be controlled under constant volume conditions.

The main reasons for the discrepancies between the simulation and experimental results can be analyzed as follows:

(1) After the test sample is used, the closed bomb device is not thoroughly cleaned, leaving some residue inside. This residue reduces the internal volume of the closed bomb device, resulting in fluctuations and higher readings in the pressure sensor data, as shown in Figure 4(b).
(2) Continuous experiments can result in a decrease in oxygen content inside the closed bomb device, leading to a lower burning rate of the test sample propellant, as shown in Figure 5(b).

To ensure the reliability of the experiment, assurance is provided from three aspects: repeatability, accuracy, and quality of data acquisition.

Repeatability: The experimental samples are divided into three groups: high temperature (+70°C), room temperature (+20°C), and low temperature (−55°C). Each group undergoes three repeated tests to ensure repeatability.

Accuracy: The results of the nine test groups are compared and analyzed with the simulated results. The experimental results are found to be consistent with the theoretical expectations, ensuring the accuracy of the experimental results.

Quality of data acquisition: The experimental samples, test equipment, and data acquisition devices used in the experiments are reliable instruments provided by Liaoning Northern Huafeng Special Chemical Co., Ltd. This ensures the high-quality collection of experimental data.

By using Equation (8), the chamber pressure $f$ can be obtained, which is only related to the peak pressure $P_{max}$ and the burning rate coefficient $u_1$ obtained from the closed bomb tests. From Figures 4 to 6, it can be observed that at +70°C, the average time for the pressure during propellant combustion to reach its peak is the shortest, approximately 2 ms; at +20°C, it is approximately 2.33 ms; and at −55°C, it is the longest, approximately 2.83 ms.

*3.2. Internal Ballistics Model.* During the separation process, the thrust generated by the propellant serves as the initial driving force for the motion of the front-stage separation body. To obtain this propulsion force, it is necessary to solve the interior ballistics of the front-stage separation body. The interior ballistics equations can provide three instantaneous parameters of the front-stage separation body at the moment of separating from the launch tube: velocity, pressure (thrust), and displacement. Velocity is a key parameter that influences the motion state of the front-stage separation body after completing the separation action. It also serves as an input parameter for studying the aerodynamic characteristics of the front-stage separation body during its flight after separation. The magnitude of velocity affects the effective detection distance of the front-stage separation body. For a detailed analysis of the effective detection distance, please refer to Section 5.3.

In this study, the front-stage separation body is secured to the launch tube using two brass shear pins with a diameter of 1.2 mm. The shear strength of the brass material is 300 MPa. Therefore, each copper shear pin exerts a shear force of 339.12 N, which translates into an ignition pressure of $P_0 = 2.54$ MPa for the front-stage separation body. The internal ballistic characteristics of the launch mechanism can be obtained by using an equivalent launch model based on the classical internal ballistic equations, as shown below [14–18]:

Table 4: Main parameters of interior ballistics.

| Parameter | Value | Parameter | Value |
|---|---|---|---|
| Launch tube diameter ($d$ (m)) | 0.022 | Covolume $\alpha$ ($m^3$/kg) | 0.001 |
| Projectile mass ($m$ (kg)) | 0.05 | Propellant charge ($\omega$ (kg)) | $2\times10^{-4}$ |
| Chamber volume ($V_0$ ($m^3$)) | $1.6\times10^{-6}$ | Burning rate index ($n$) | 1 |
| Launch tube length ($l_g$ (m)) | 0.008 | Types of propellant | $C_6H(NO_2)_3O_2Pb\cdot H_2O+BPN$ |
| Projectile starting pressure ($P_0$ (MPa)) | 2.54 | Propellant density $\rho$ (kg/$m^3$) | 1,100 |
| Thermal coefficient of propellant ($\theta$) | 0.5 | Cutting force per copper pin ($F_c$ (N)) | 339.12 |
| Copper pin diameter ($r_c$ (mm)) | 1.2 | Cutting strength of copper pins ($P_c$ (MPa)) | 300 |

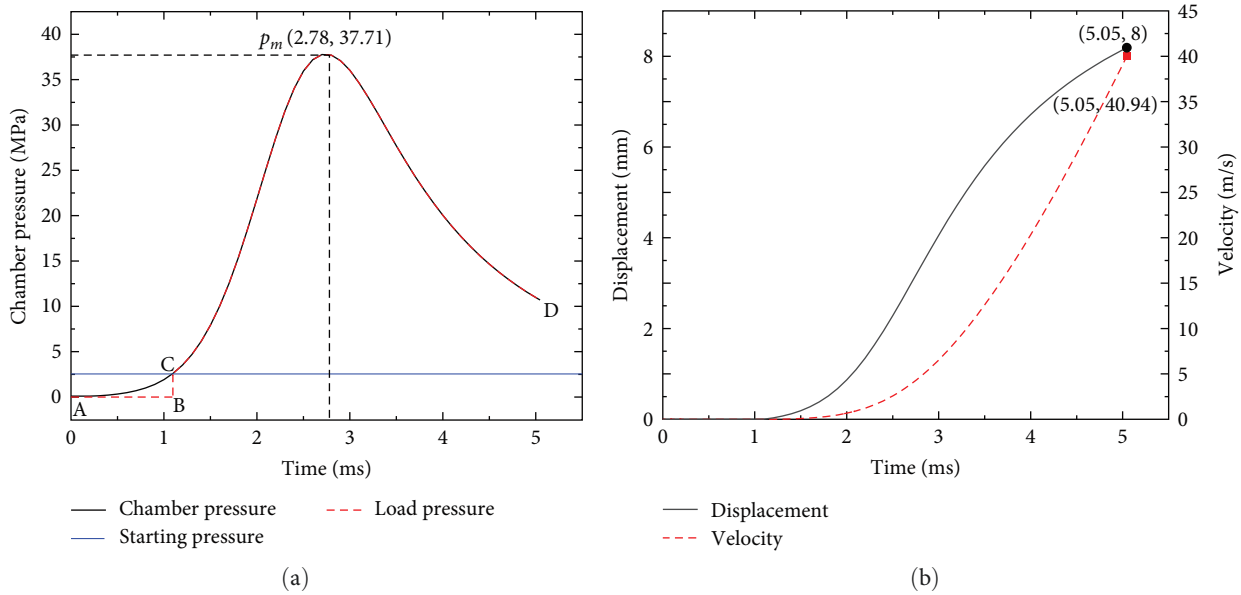


Figure 7: Interior ballistics curves: (a) chamber pressure curves; (b) displacement and velocity curves.

$$\begin{cases} \psi = \chi z(1+\lambda z+\mu z^2), \\ \dfrac{dz}{dt} = \dfrac{u_1}{e_1}p^n, \\ \varphi m\dfrac{dv}{dt} = SP, \\ \dfrac{dl}{dt} = v, \\ SP(l_\psi + l) = f\omega\psi - \dfrac{\theta}{2}\varphi m v^2, \end{cases} \tag{9}$$

where $\psi$ represents the mass fraction burned of the propellant; $\chi$, $\lambda$, $\mu$ are shape characteristics of the propellant, which depend solely on its shape and dimensions; $z$ represents the relative thickness of the propellant; $t$ represents time; $u_1$ represents the burning rate coefficient; $e_1$ represents half of the original thickness of the propellant grain; $P$ represents gas pressure; $n$ is the burning exponent; $\varphi$ represents the secondary work coefficient; $m$ represents the mass of the front-stage separation body; $v$ represents the velocity of the front-stage separation body; $S$ represents the cross-sectional area of the launch tube; $l$ represents the displacement of the front-stage separation body; $l_\psi$ represents the contraction length of the free volume in the combustion chamber; $f$ represents the propulsive force generated by the propellant; $\omega$ represents the mass of the propellant; $\theta$ represents the adiabatic coefficient. The main calculation parameters for the above internal ballistic equations are shown in Table 4.

As shown in Figure 7(a), taking the internal ballistic results at +22°C as an example, the duration of the barrel pressure of the launch tube is 5.05 ms, and the maximum chamber pressure $P_m$ is 37.71 MPa. When the pressure generated by the combustion of the propellant in the chamber is less than the ignition pressure of the front-stage separation body, the front-stage separation body remains stationary, as shown in segments A–C of Figure 7(a); when the pressure generated by the propellant in the chamber is greater than the ignition pressure of the front-stage separation body, the front-stage separation body begins to move, as shown in segment C—$P_m$ of Figure 7(a). At this time, the effect of the gas generation rate of the propellant on the chamber pressure is greater than the effect of the increase in chamber volume after the motion of the front-stage separation body, and the pressure curve continues to rise until these two

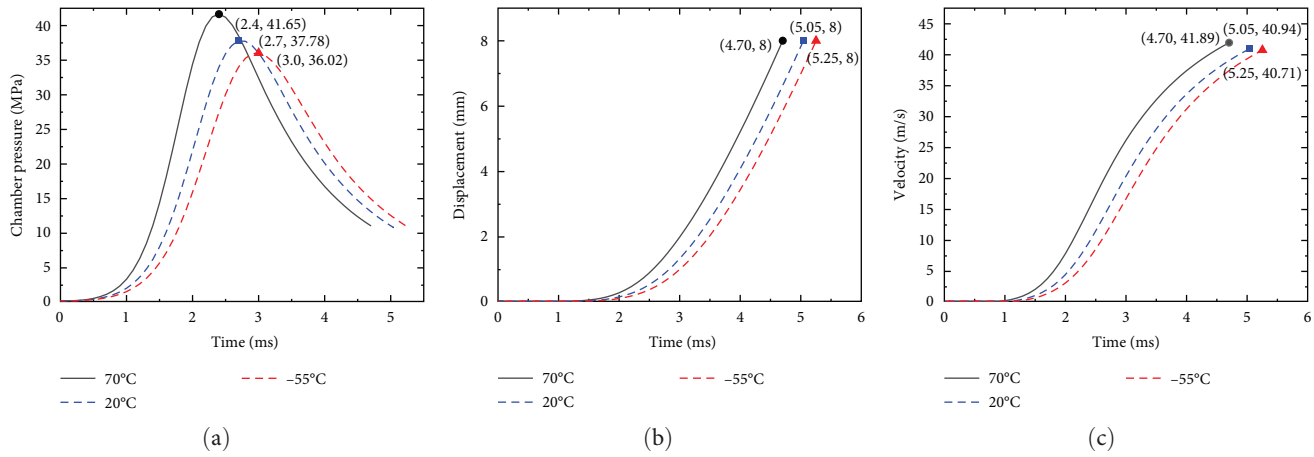


Figure 8: Interior ballistics curves at different temperatures: (a) chamber pressure curves; (b) displacement curve; (c) velocity curves.

effects reach a balance, and the chamber pressure reaches the maximum value $P_m$. With the continuous acceleration of the front-stage separation body, its acceleration and velocity also increases continuously. After the front-stage separation body starts to move, the effect of the increase in chamber volume becomes dominant over the effect of the gas generation rate, and the chamber pressure begins to decrease. The acceleration of the front-stage separation body decreases with the decrease in chamber pressure, but the velocity of the front-stage separation body continues to increase until it is completely separated from the launch tube. This is shown in segments $P_m$—D of Figure 7(a) and the velocity curve in Figure 7(b).

As mentioned earlier, the front-stage separation body is initially secured by two symmetric copper pins before launch. Only when the chamber pressure exceeds the initiation pressure does the front-stage separation body start to move. Therefore, the chamber pressure acting on the front-stage separation body, loaded with the pins, is represented as A–B–C and C–D in Figure 7(a).

As shown in Figure 7(b), the length of the internal ballistic of the launch tube is 8 mm, and the maximum velocity of the front-stage separation body when it separates from the launch tube is 40.94 m/s. Since the chamber pressure at the initial combustion of the propellant does not exceed the initiation pressure $P_0$, the displacement and velocity of the front-stage separation body are approximately zero at the initial moment. When the chamber pressure exceeds the initiation pressure $P_0$, the two copper pins are sheared, and the front-stage separation body begins to move until it completely separates from the launch tube. The internal ballistic curves at different temperatures are shown in Figure 8.

## 4. External Ballistic Aerodynamic Simulation of the Front-Stage Separation Body

Studying the dynamic coefficients, drag, lift, and other forces experienced by the front-stage separation body during flight is a necessary condition for investigating whether the front-stage separation body can successfully separate, and it serves as input for calculating the separation dynamics model of the front-stage separation body.

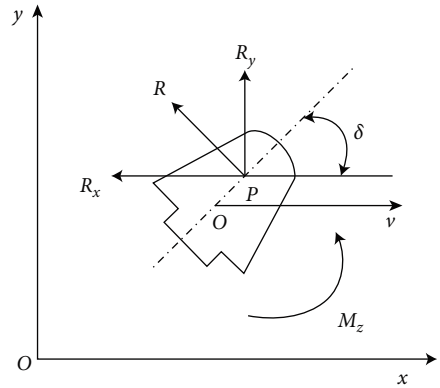


Figure 9: Schematic diagram of overall aerodynamic forces.

*4.1. Force Analysis on the Front-Stage Separation Body.* Once the front-stage separation body completes its separation, the propellant thrust immediately disappears and is mainly influenced by the total aerodynamic forces.

As shown in Figure 9, the total aerodynamic force $R$ can be decomposed into horizontal component $R_x$ and vertical component $R_y$ (or along the axial direction of the front-stage separation body, it can be decomposed into axial force $R_A$ and normal force $R_n$ perpendicular to the axial direction). Due to the presence of the pitching moment $M_z$, the front-stage separation body will generate an angle of attack $\delta$ during its flight. Where $P$ represents the pressure center, and $O$ represents the center of mass. The positive directions of the coordinate system are all based on the positive direction of the $X$-axis.

*4.2. Aerodynamic Force Model.* The relationship between $R_x$, $R_y$, $R_A$, and $R_n$ can be obtained from Figure 9.

$$\begin{cases} R_x = R_A \cos\delta + R_n \sin\delta, \\ R_y = R_n \cos\delta - R_A \sin\delta. \end{cases} \tag{10}$$

Table 5: Simulation condition parameter settings.

| Medium | Absolute pressure (Pa) | Grid model | Mach number | Temperature (K) | Rpm |
|---|---|---|---|---|---|
| Ideal gas | 101,325 | Slip grid | 0.9 | 300 | 10,062 |

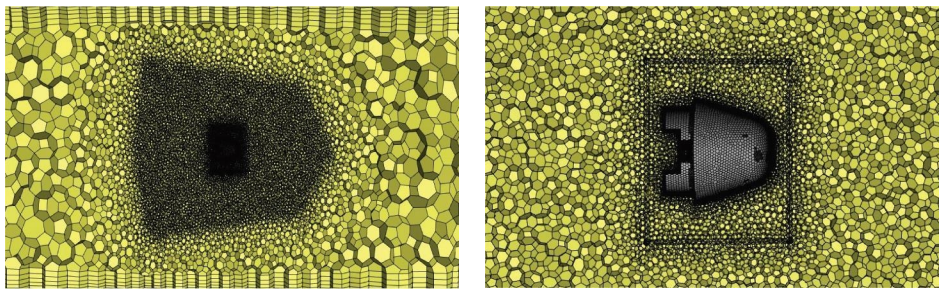

(a) (b)

Figure 10: Schematic diagram of the computational grid for the model shape: (a) overall schematic diagram of the computational grid; (b) boundary schematic diagram of the computational grid.

The moment of the total aerodynamic force $R$ on the center of mass of the front-stage separation body is as follows:

$$M_z = \frac{\rho v_k^2}{2} SLm_z, \tag{11}$$

where $\rho$ represents the air density at separation altitude; $v_k$ represents the flight speed of the separated body relative to the air; $S$ represents the maximum windward area of the separated stage; $L$ is the reference length, often taken as the specific model's length or diameter; $m_z$ is the static moment coefficient.

By replacing the total aerodynamic force $R$ with $R_x$ and $R_y$, we can obtain the relationship between the pitching moment $M_z$ and the drag $R_x$, lift $R_y$, aerodynamic center $P$, and center of mass $O$ in terms of $h$. It can be expressed as follows:

$$\begin{cases} M_z = \left(R_y \cos\delta + R_x \sin\delta\right)h, \\ m_z = \left(C_y \cos\delta + C_x \sin\delta\right)\dfrac{h}{L}. \end{cases} \tag{12}$$

*4.3. Aerodynamic Simulation.* Researchers typically employ wind tunnel testing, experimental measurement methods, and CFD numerical simulations to explore the aerodynamic performance of projectiles. Wind tunnel testing involves complex testing conditions and is relatively expensive. Experimental measurement methods are often limited by the precision of data measurements. CFD numerical simulation techniques offer advantages such as lower cost, the ability to simulate complex flow fields, and predict fluid behavior [19, 20]. Therefore, this study chooses CFD numerical simulation to obtain the aerodynamic parameters of the front-stage separation body.

Based on the analyses in Sections 4.1 and 4.2, the aerodynamic coefficients, drag, lift, etc., of the front-stage separation body at different angles of attack are obtained through simulation. These values serve as inputs for studying the separation process of the front-stage separation body.

The computational model employed uses the SST (shear stress transport) $K$–$\omega$ model, which has good adaptability for handling different interfaces and exhibits good convergence [21–23]. The simulation conditions are set, as shown in Table 5.

The computational grid for the shape of the front-stage separation body is shown in Figure 10.

As shown in Figure 10(a), the overall computational grid for the front-stage separation body employs a polyhedral mesh that combines structured and unstructured grids. The adaptability of polyhedral meshes is stronger, allowing for flexible adjustment of mesh size and shape in the flow area to more accurately capture details and boundary features in the flow field. The geometric flexibility is great, making it easier to handle unconventional geometric shapes, bringing simulation results closer to reality. In terms of grid quality, it can provide a more uniform grid distribution, avoiding singularities and distortion problems in structured grids. In Figure 10(b), the grid near the front-stage separation body is refined, with 280 grid points arranged in the flow direction and 270 grid points arranged normally to it. The arrangement of the normal points ensures that the first layer mesh grid $y^+ < 5$. To investigate the influence of different grid quantities on the simulation results, this study generated four sets of grids while ensuring grid refinement. The grid quantities are as follows: $2.3 \times 10^5$, $1.2 \times 10^6$, $2.0 \times 10^6$, and $2.7 \times 10^6$. Figure 11 presents the impact of different grid quantities on the drag coefficient ($C_d$) of the front-stage separation body.

As shown in Figure 11, when the mesh quantity reaches $2.0 \times 10^6$, the variation in the coefficient of drag ($C_d$) is minimal. Therefore, to balance computational resources and ensure the accuracy of simulation calculations, a mesh quantity of $2.0 \times 10^6$ will be used in subsequent simulations.

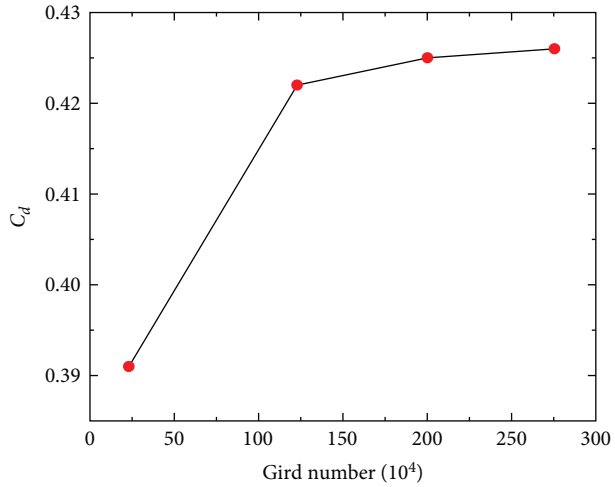


FIGURE 11: Influence of different mesh quantities on the $C_d$.

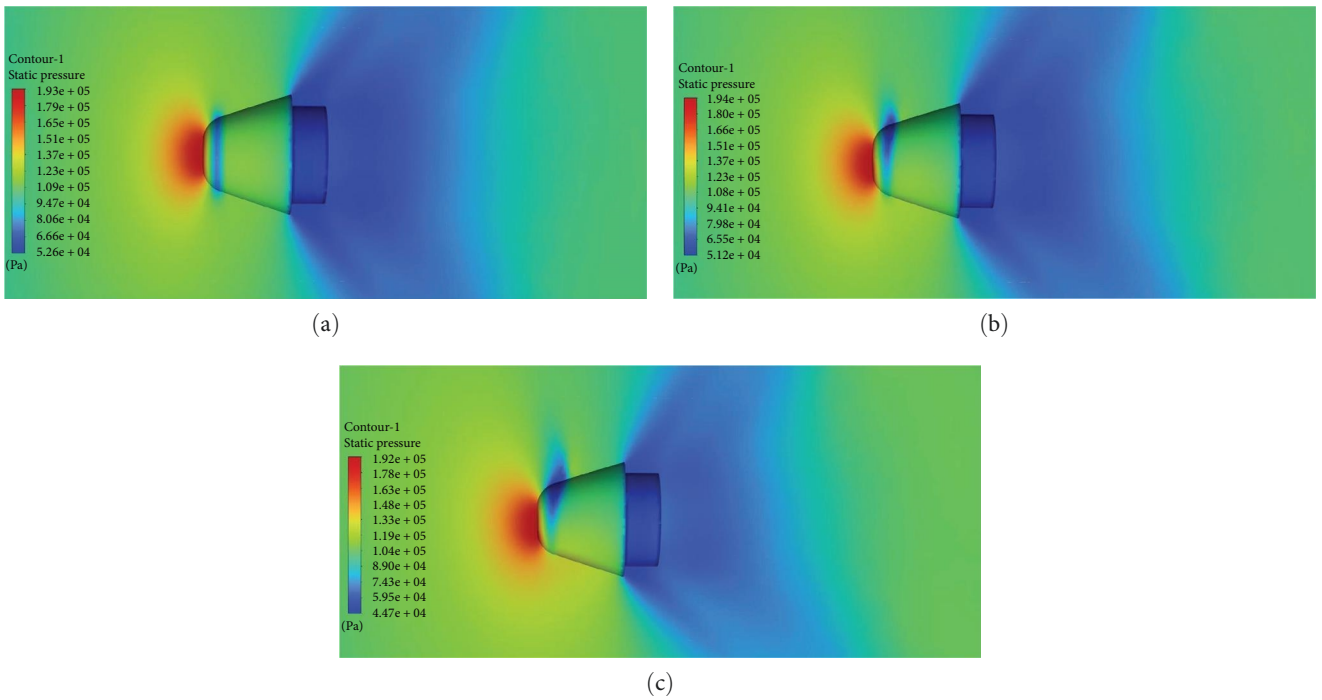


FIGURE 12: Pressure contour map: (a) 0°; (b) 4°; (c) 8°.

For a projectile relying on rotational stability, maintaining an angle of attack within 10° is considered ideal [24]. Moreover, to investigate the influence of the angle of attack variations on CFD simulation results, angles of attack were set at 0°, 4°, and 8°, respectively. By conducting simulations, pressure contour maps corresponding to different angles of attack can be obtained, as shown in Figure 12(a)–12(c).

As shown in Figure 12(a), when the angle of attack is 0°, the lift distribution on the head of the front-stage separation body is uniform, and the pressure center is almost parallel to the axis of the front-stage separation body. This configuration exhibits the best flight stability and represents the most ideal flight attitude. In Figure 12(b), with an angle of attack of 4°, there is a certain angle between the pressure center and the axis of the front-stage separation body. A low-pressure region appears above the head of the front-stage separation body. The formation of pressure difference can cause deviations from the original flight trajectory during the flight of the front-stage separation body. In Figure 12(c), with an angle of attack of 8°, the angle between the pressure center and the axis of the front-stage separation body increases further. The increasing pressure difference deteriorates the flight stability of the front-stage separation body even more.

Additionally, aerodynamic parameters for different angles of attack of the front-stage separation body are presented in Table 6.

Table 6: Aerodynamic parameters for different angles of attack.

| $\delta$ (°) | $C_d$ | $C_L$ ($10^{-4}$) | $R_x$ (N) | $R_y$ (N) | $R_z$ (N) |
|---|---|---|---|---|---|
| 0 | 0.43 | 1.78 | 17.8 | 0.008 | 0.025 |
| 4 | 0.44 | 8.39 | 18.8 | 0.033 | 0.042 |
| 8 | 0.44 | 10.24 | 18.9 | 0.040 | 0.060 |

*Note.* $C_d$ represents the drag coefficient, $C_L$ represents the lift coefficient, $R_x$ represents the drag force, $R_y$ represents the lift force, and $R_z$ represents the side force.

As shown in Table 6, the $C_d$ remains relatively unchanged as the angle of attack increases, while the $C_L$ shows a more noticeable increase. Therefore, there is no significant causal relationship between drag and angle of attack variations. However, with an increasing angle of attack, both lift and side force also increase; this would inevitably lead to an unstable flight attitude. Therefore, for the separation mechanism in this paper, a smaller attack angle is more advantageous in achieving the desired effect.

According to the literature [21], we can learn that the attack angle affects the stability of a spinning projectile. A smaller attack angle is usually beneficial for maintaining the stable flight of the spinning projectile because it reduces the relative velocity between the projectile and the airflow, thereby reducing unstable aerodynamic effects. However, a too-large attack angle may decrease the stability of the spinning projectile, making it more susceptible to disturbances and yawing. The attack angle also has a significant impact on the ballistic characteristics of the spinning projectile. A smaller attack angle typically increases the range and flight distance of the spinning projectile. This is because a smaller attack angle reduces drag and provides better aerodynamic performance. On the contrary, a larger attack angle may decrease the range and flight distance of the spinning projectile as it increases drag and reduces flight speed. The attack angle also affects the rotational dynamics of the spinning projectile. Different attack angles result in variations in the distribution of aerodynamic forces and moments on the projectile, which in turn affect the rotational rate and stability of the projectile's axis of rotation.

The increased lift and side force contribute to a more pronounced Magnus effect on the front-stage separation body, with lift having a more significant impact compared to side force [25, 26]. Therefore, it is essential to consider how to ensure that the angle of attack of the front-stage separation body remains within a reasonable range during the design process of practical engineering applications.

## 5. Analysis of the Dynamic Characteristics of Separation

The focus of this section is on the velocity increment of the front-stage separation body and the displacement difference generated by the two-stage separation bodies within the effective time. Since the impact of the Magnus effect on spin-stabilized projectiles is inevitable, it is also crucial to ensure that the Magnus force remains within a reasonable range. This study primarily evaluates the Magnus effect on the front-stage separation by observing the variations in the angle of attack.

*5.1. Model Simplification.* To facilitate the simulation calculation of the separation dynamics model, it is necessary to make reasonable simplifications to the model.

(1) Both the front-stage separation body and the main body are treated as undeformed rigid bodies.
(2) The propellant thrust provided by the annular ejection propellant container is simplified as a constant value.
(3) The projectile has a range of approximately 10 km, with an initial separation altitude of about 100 m from the ground. The effects of Earth's curvature, rotational speed, and launch latitude are not considered after separation.
(4) After separation, the front-stage separation body is assumed to be influenced only by aerodynamic forces, wire tension, and gravity.
(5) Due to the low separation altitude and short duration of the separation action, the influence of crosswinds is not considered.
(6) During the separation process, the rotational speeds of the two-stage separation bodies are assumed to be equal, and the torque generated by wire rotation and wire deformation is neglected in a short time.

*5.2. Separation Dynamics Model.* Assuming the mass of the front-stage separation body is $m$, moments of inertia and products of inertia are $J$ ($J_x$, $J_y$, $J_z$, $J_{xy}$, $J_{xz}$, $J_{yz}$), the external forces acting on it are $F$ ($F_x$, $F_y$, $F_z$), the moments about the center of mass are $M$ ($M_x$, $M_y$, $M_z$), the displacement of the center of mass is represented by $r$ ($r_x$, $r_y$, $r_z$), and the angular velocity about the center of mass is $\omega$ ($\omega_x$, $\omega_y$, $\omega_z$), Therefore, the six-degree-of-freedom dynamic equations for the front-stage separation body can be obtained as follows [27, 28]:

$$\begin{cases} m\ddot{r} = F, \\ J \cdot \dot{\omega} + \omega \times J \cdot \omega = M. \end{cases} \tag{13}$$

The relationship between the rotational angular velocity $\omega$ ($\omega_x, \omega_y, \omega_z$) of the front-stage separation body and its Euler angle rates ($\dot{\varphi}, \dot{\gamma}$) is as follows:

$$\begin{cases} \dot{\varphi} = \dfrac{1}{\cos\varphi}\left(\omega_y \sin\gamma + \omega_z \cos\gamma\right), \\ \dot{\psi} = \omega_y \cos\gamma - \omega_z \sin\gamma, \\ \dot{\gamma} = \omega_x - \tan\psi\left(\omega_y \sin\gamma + \omega_z \cos\gamma\right). \end{cases} \tag{14}$$

During the separation process, the axial separation of the two separable bodies can be divided into an active segment and a passive segment.

Step 1: Active separation segment

After receiving the separation command, the propellant inside the annular ejection propellant container will rapidly generate a certain amount of high-pressure gas. As the pressure inside the chamber continues to increase, the copper shear pin will be sheared, and the front-stage separation body will start accelerating. The acceleration before it separates from the internal barrel is called the active separation phase. During this phase, the front-stage separation body is mainly influenced by gravity $G$, total aerodynamic force $R$, propellant thrust $F_f$, frictional force $f_N$, and wire tension force $f_d$. Where the gravity $G$ is related to the mass $m$ and determines the response of the front-stage separation body to external forces. The total aerodynamic force $R$ causes instability in the motion of the front-stage separation body, thereby affecting its trajectory. The propellant thrust $F_f$ generated by the propellant directly influences the motion state and velocity of the front-stage separation body. In this model, it is assumed that the thrust force disappears instantaneously once the separation is completed. The frictional force $f_N$ arises when the front-stage separation body comes into contact with the surface of the launch tube, hindering its motion and affecting its trajectory and velocity. The wire tension force $f_d$ refers to the pulling force parallel to the wire as the front-stage separation body is pulled outward along the wire. In this model, it is considered to primarily impede the flight of the front-stage separation body, influencing its flight velocity.

Step 2: Passive separation segment

After the front-stage separation body separates from the internal barrel, it enters the passive separation phase. At this point, the front-stage separation body is almost completely detached from the main body and is primarily influenced by gravity $G$, total aerodynamic force $R$, wire tension force $f_d$, and the post-effect of the propellant gas force $f_h$. Where the post-effect of the propellant gas force $f_h$ refers to various impacts and effects caused by the high-temperature and high-pressure gases generated during the combustion process of the propellant at the moment of separation between the front-stage separation body and the main body, it affects the flight speed and attitude of the front-stage separation body.

During the separation process, the propellant thrust $F_f$ is perpendicular to the separation plane. The posteffect of the propellant gas force $f_h$ is a time-varying force, with its maximum impact on projectile acceleration being around 3% [29]. During simulation calculations, the posteffect of the propellant gas force can be directly equivalent to velocity increment. The variations in external forces acting on the front-stage separation body in different stages are as follows:

$$\begin{cases} F_1 = G + R + F_f + f_d + f_N & (\text{step } 1), \\ F_2 = G + R + f_d + f_h & (\text{step } 2). \end{cases} \tag{15}$$

Similarly, the variations of external torque acting on the front-stage separation body in each stage are as follows:

$$\begin{cases} M_1 = M_R + M_{F_f} + M_{f_d} & (\text{step } 1), \\ M_2 = M_R + M_{f_d} + M_{f_h} & (\text{step } 2), \end{cases} \tag{16}$$

where $M_R$ represents the aerodynamic torque, $M_{Ef}$ represents the propellant torque, $M_{fd}$ represents the wire tension torque, and $M_{fh}$ represents the aftereffect of propellant gas torque.

In stage 1, both the propellant thrust $F_f$ and the wire tension force $f_d$ are parallel to the axial line of the front-stage separation body, and the front-stage separation body is always subject to rigid constraints. Therefore, the force arm and angle corresponding to the propellant thrust $F_f$ and wire tension force $f_d$ are both zero, resulting in $M_f$ and $M_{fd}$ being equal to zero. Therefore, Equation (16) can be simplified as follows:

$$\begin{cases} M_1 = M_R & (\text{step } 1), \\ M_2 = M_R + M_{f_d} + M_{f_h} & (\text{step } 2). \end{cases} \tag{17}$$

To validate the accuracy of the model for the motion state after separation, we plan to evaluate the model's accuracy through a comparison analysis between simulation results and experimental data. The theoretical model and simulation results have been provided in this paper, but due to project constraints, actual projectile-firing validation experiments have not been conducted yet. In future research, we will explore the evaluation and optimization of the separation dynamics model as a separate research topic.

*5.3. Result.* Based on the theoretical analysis in Sections 5.1 and 5.2, experimental data from Section 3, and simulation results from Section 4, the entire separation process of the separation mechanism is simulated and calculated using ADAMS. The corresponding parameter results after separation are obtained, including the displacement variation of the two-stage separation bodies, the velocity variation of the front-stage separation body, and the change in the angle of attack of the front-stage separation body after completion of separation. The initial velocity for the simulation is set to 300 m/s, and the rotational speed is set to 10,062 rpm.

As shown in Figure 13(a), the front-stage separation body instantaneously shears the copper shear pin under the effect of propellant thrust. After 0.5 s, it travels a distance of 156.5 m. This means that within 0.5 s after completing the separation action, the front-stage separation body can ensure that its position remains ahead of the main body and does not collide with it. After 0.5 s, the displacement of the main body begins to exceed that of the front-stage separation body, indicating that if the trajectory of the front-stage separation body does not deviate significantly, it will collide with the main body after 0.5 s.

The main reason for the collision is that the main body has a much stronger kinetic energy storage capacity compared to the front-stage separation body. The mass of the main body (approximately 21.76 kg) is much greater than that of the front-stage separation body (approximately 50 g). According to the law of conservation of momentum, the velocity of the

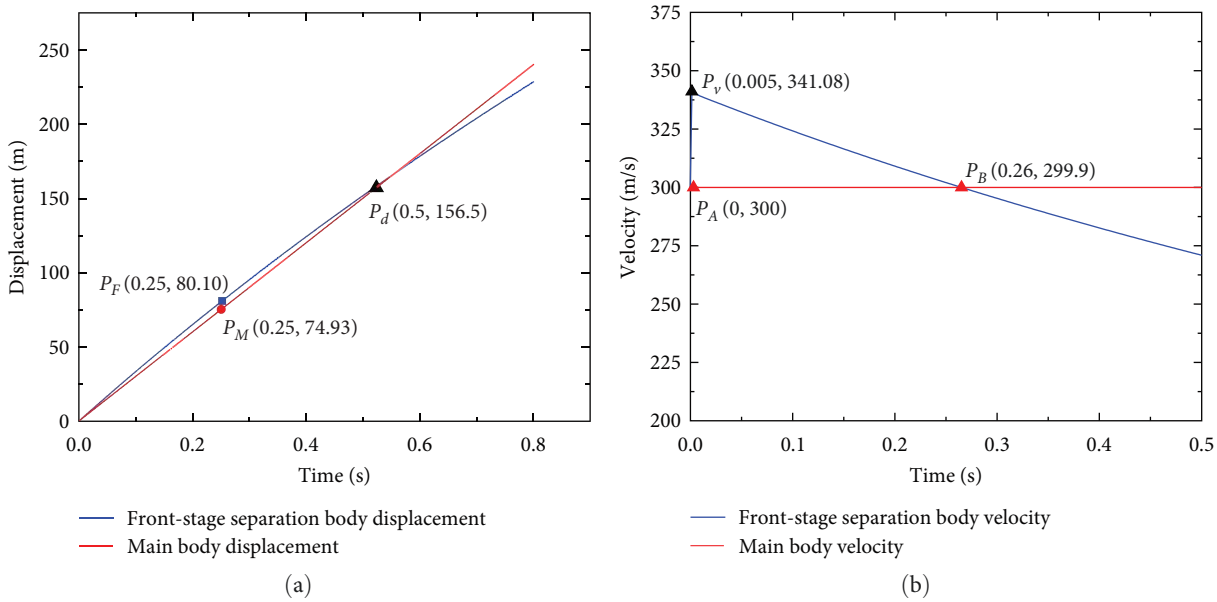


Figure 13: Simulation results of displacement and velocity: (a) displacement curve; (b) velocity change curve.

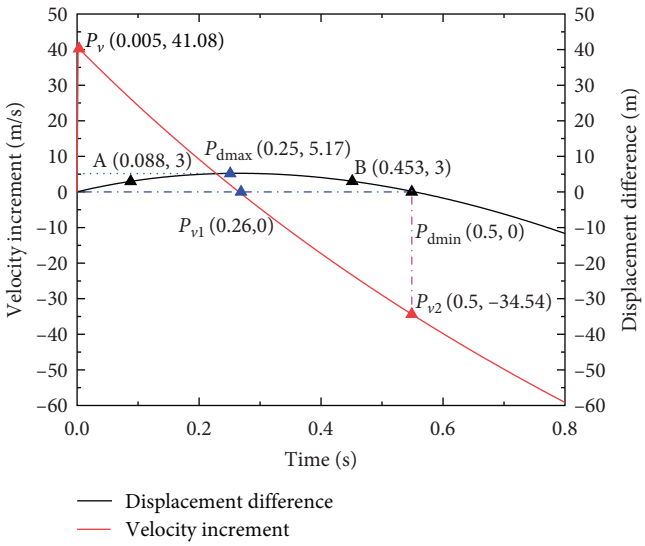


Figure 14: Velocity increment and displacement difference curve.

main body after the separation mechanism completes separation is approximately 299.906 m/s, while the velocity of the front-stage separation body will continuously decrease after 0.005 s and becomes lower than that of the main body after 0.26 s. This observation is consistent with the results shown in Figure 13(b).

By subtracting the displacement from Figure 13(a) and the velocity from Figure 13(b), the motion variations of the two-stage separation bodies can be better understood. As shown in Figure 14, the maximum velocity increment of the front-stage separation body occurs at point $P_v$, with a value of 41.08 m/s. This result is in good agreement with the velocity results in Figure 8(c), with an average error of approximately 1.07%. This confirms the correctness of the dynamic simulation. The main reasons contributing to the average error are as follows: Figure 8(c) represents the calculation results using MATLAB, while the value of $P_v$ in Figure 14 corresponds to the results obtained using ADMS. The use of different computational tools can introduce varying rounding errors and truncation errors during numerical approximation and discretization calculations. Additionally, differences in handling model assumptions, parameter settings, and the choice of algorithms and numerical techniques for solving the dynamical model can also impact the accuracy and precision of the model calculation results. To minimize the average error, validation, and calibration can be performed during the model design and calculation process, utilizing precise parameters and algorithms to enhance the accuracy of the computed outcomes.

Point $P_{dmax}$ corresponds to the maximum displacement difference (maximum explosion height) between the two stages, with a value of 5.17 m. At this point, the velocity increment has decreased from 41.08 m/s at point $P_v$ to 0 m/s at point $P_{v1}$. As the velocity continues to decrease, the displacement difference also decreases. After 0.5 s, the displacement difference reaches 0 m at point $P_{dmin}$, while the velocity increment has decreased from point $P_v$ to point $P_{v2}$, resulting in a reduction of 34.54 m/s compared to the initial separation velocity of 300 m/s.

The range of explosion heights for the rotating projectile studied in this paper is 3–10 m. According to project requirements, separation should begin when the target is 100 m away. Also, since the speed attenuation of the projectile body at the end of the trajectory is almost zero, its motion state at the end of the trajectory can be equivalent to uniform rectilinear motion, allowing an estimation that the time it takes for the projectile body to hit the ground target is approximately 0.33 s, which means that the effective separation time required for the entire separation process must be less than 0.33 s. As shown in Figure 14, when the projectile

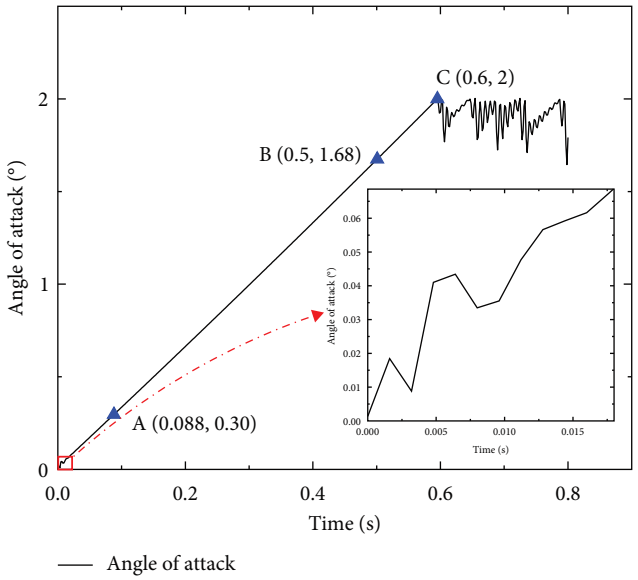


FIGURE 15: Curve of attack angle variation.

reaches a maximum explosion height of 5.17 m, the corresponding time is 0.25 s, indicating that the separation mechanism can complete the separation action within 0.33 s and enable the projectile to achieve the maximum explosion height. The projectile's explosion height between points A and B is greater than 3 m, with point A corresponding to a time of 0.088 s, so the projectile's explosion height remains above 3 m in the time interval (0.088 and 0.33 s). As shown in Figure 13(a), at 0.25 s, the front separation body has flown approximately 80.1 m, while the main body has flown about 74.93 m. At 0.5 s, both the main body and the front separation body have traveled about 156.5 m, meaning that the two-stage separation bodies will never collide with each other within the 100 m separation task distance. When the projectile starts to separate from the target 100 m away, the distance between the two will always remain within (3 and 5.17 m). In practical engineering applications, a time of 0.242 s can fully meet the requirements of the detonator control circuit because the current 32-bit microcontroller systems operate at the megahertz level; they can make distance judgments 3–5 times continuously in 10 ms intervals or even more. Therefore, the time interval between the two stages of the separation mechanism is reasonable and can meet the requirements of the actual task. An unreasonable time interval will result in the projectile failing to achieve the desired explosion height. For example, premature separation may cause the two-stage separation bodies to collide in the air, or even the main body may hit the target earlier than the front separation body, leading to mission failure.

As shown in Figure 15, the maximum value of the attack angle for the front-stage separation body during its flight after separation is approximately 2°. According to the design requirements of the separation mechanism, the effective working time is between point A and point B. During this time, the maximum attack angle of the front-stage separation body is 1.68°. This means that the maximum change in the attack angle of the front-stage separation body before it impacts the target or obstacles in the target area will not exceed 1.68°, ensuring the flight stability of the front-stage separation body after separation. At point C, there is an oscillation phenomenon in the attack angle. The main reason for this is that the front-stage separation body stabilizes its flight attitude through the spin. The decrease in velocity reduces the angular momentum, weakens the spin stability, and leads to the occurrence of a jitter in the flight attitude.

The zoomed-in result in Figure 15 shows the variation of the attack angle for the front-stage separation body at the moment of detachment from the main body. Due to the influence of the post-effect of the propellant gas force $f_h$, the front-stage separation body experiences oscillations in the initial stage of separation, resulting in significant fluctuations in the attack angle. However, around 0.015 s later, the influence of the post-effect of the propellant gas force $f_h$ gradually diminishes, and the change in the attack angle tends to stabilize.

## 6. Conclusions

(1) The proposed end-detection separation mechanism for spinning projectiles, with its unique design concept and operating mechanism, differs from the current proximity fuzes. This research achievement provides new design ideas and a theoretical foundation for fuze researchers to explore the design of detection and separation mechanisms under spinning conditions.

(2) Based on data from closed bomb tests and CFD aerodynamic simulations, the dynamic characteristics of the separation mechanism were investigated using ADAMS. The separation dynamic model was verified by comparing it with the velocity increment of the front-stage separation body.

(3) Because the operation of this separation mechanism does not rely on electromagnetic waves, lasers, infrared, etc., and mainly utilizes wires for signal transmission, it possesses the capability to be completely insensitive to interference sources such as electromagnetic disturbances, strong heat sources, rain, snow, and sandstorms. In the future, it can be used in conjunction with current proximity fuzes, expanding the applicability range of proximity munitions and enhancing their resistance to interference. This will further enhance the effectiveness of proximity munitions.

## Data Availability

If data are required, please contact the author via E-mail: 2111620964@stu.sylu.edu.cn.

## Conflicts of Interest

The authors declare that they have no conflicts of interest.

## Authors' Contributions

Lei Zhao has contributed to the writing—original draft, methodology, investigation, experimentation, and visualization. Shuai Yue has contributed to the methodology, investigation, reviewing and editing, and funding acquisition. Zhong-hua Du has contributed to the methodology, investigation, project management, and funding acquisition. Teng-fei Ma has contributed to the resources. Xing-xiao Li has contributed to the experimentation.

## Acknowledgments

Very grateful for the patient help and professional guidance given by the review experts, Academic Editor Babak Shotorban, and Editorial Assistant Andrew Mendoza throughout the entire manuscript handling process. The project was supported by (1) National Natural Science Foundation of China (52102436); (2) China Postdoctoral Science Foundation (2020M681615); (3) Natural Science Foundation of Jiangsu Province (BK20200496); (4) Open Fund of Key Laboratory of Impact and Safety Engineering, Ningbo University (CJ202107); (5) Shanghai Natural Science Foundation (23ZR1462700); (6) National Key Laboratory Open Fund for Strength and Structural Integrity (ASSIKFJJ202304006); (7) Postgraduate Research & Practice Innovation Program of Jiangsu Province (KYCX23_0508).

## References

[1] Z.-P. Chen, H.-J. Li, B.-Q. Yan, C.-H. Zhang, S.-X. Qiao, and H. Zhang, "Control method of millimeter-wave proximity fuse burst height based on data calibration for tank guns," *Acta Armamentarii*pp. 1–12, 2023.

[2] H. Zhang and K. Dai, "Development and prospect of advanced fuse technology," *Chinese Science Bulletin*, vol. 68, no. 25, pp. 3293–3310, 2023.

[3] B. He, Y. Yuan, J. Ren et al., "A high-functional-density integrated inertial switch for super-quick initiation and reliable self-destruction of a small-caliber projectile fuze," *Micromachines*, vol. 14, no. 7, pp. 1377–1384, 2023.

[4] L.-F. Guo and Z. Zhao, "Theoretical and experimental study on separation dynamics of pyrotechnic separation mechanism for spacecraft," in *Proceedings of the 10th National Conference on Multibody Dynamics and Control and the 5th National Conference on Aerospace Dynamics and Control, edited by the Dynamics and Control Committee of the Chinese Society of Theoretical and Applied Mechanics and the Aerospace Dynamics and Control Committee of the Chinese Society of Theoretical and Applied Mechanics*, p. 50, School of Aeronautic Science and Engineering, Beihang University, Beijing, 2017.

[5] L.-F. Qian, *Ballistics of Artillery Projectiles*, Beijing Institute of Technology Press, Beijing, 2017.

[6] S.-H. Xiong, T. Yang, Y.-J. Wu, J.-C. Wang, Y. Li, and Y.-Q. Wen, "Numerical simulation of radiated noise during combustion of energetic materials in a closed bomb," *Defence Technology*, vol. 18, no. 7, pp. 1167–1178, 2022.

[7] H.-T. Li, *Study on the separation dynamics and inverse problems of submarine-launched ballistic missiles*, PhD dissertation, Harbin Institute of Technology.

[8] Q. Liu, W.-T. Wang, and W.-F. Zhang, "Study on buffering performance of thin-walled metal tube with different angles," *Defence Technology*, vol. 14, no. 6, pp. 702–708, 2018.

[9] L. Liu and J.-N. Wang, "Establishment and simulation of two-stage separation bodies dynamics model for spinning projectiles," *Journal of Beijing Institute of Technology*, vol. 2, pp. 108–111+120, [In Chinese], 2005.

[10] B. N. Rao, D. Jeyakumar, K. K. Biswas, S. Swaminathan, and E. Janardhana, "Rigid body separation dynamics for space launch vehicles," *The Aeronautical Journal*, vol. 110, no. 1107, pp. 289–302, 2006.

[11] E. Al Shami and X. Wang, "Performance prediction and design parameters sensitivity analysis of two-body point absorber wave energy harvesters," *Ocean Engineering*, vol. 286, no. Part1, Article ID 115538, 2023.

[12] G. Ouaidat, A. Cherouat, R. Kouta, and D. Chamoret, "Study of the effect of mechanical uncertainties parameters on the performance of PEMFC by coupling a 3D numerical multiphysics model and design of experiment," *International Journal of Hydrogen Energy*, vol. 47, no. 56, pp. 23772–23786, 2022.

[13] H. Krier and M. Summerfield, "Interior ballistics of guns," in *Progress in Astronautics and Aeronautics*, New York University, New York, 1979.

[14] W.-H. Shi, S. Yue, C.-B. Wu et al., "Temperature influences of the recoil characteristics for aluminum honeycomb buffer in the tether-net launcher," *Defence Technology*, vol. 29, pp. 39–54, 2023.

[15] J.-G. Wang, Y.-G. Yu, L.-L. Zhou, and R. Ye, "Numerical simulation and optimized design of cased telescoped ammunition interior ballistic," *Defence Technology*, vol. 14, no. 2, pp. 119–125, 2018.

[16] Y.-W. Wang, W.-F. Zhu, J.-W. Di, and X.-H. Hu, "Study on the analysis method on ballistic performance of deterred propellant with large web size in large caliber artillery," *Defence Technology*, vol. 14, no. 5, pp. 522–526, 2018.

[17] W. Shi, S. Yue, Z. Liu, Z. Liu, Z. Du, and G. Gao, "Dynamics analysis and experimental validation of the aluminum honeycomb buffer in the tether-net launcher," *Advances in Space Research*, vol. 70, no. 11, pp. 3405–3417, 2022.

[18] S. Yue, M.-S Li, Z. Zhao, Z.-H Du, C.-B. Wu, and Q.-Z Zhang, "Parameter analysis and experiment validation of deployment characteristics of a rectangular tether-net," *Aerospace*, vol. 10, no. 2, Article ID 115, 2023.

[19] Q.-L Hui, *Experimental Aerodynamics*, National Defense Industry Press, Beijing, [In Chinese], 2000.

[20] W.-C Chen, "*Calculation of aerodynamic forces on spinning projectiles and optimization design of aerodynamic exteriors*," Master's thesis, Nanjing University of Science and Technology, 2011.

[21] N.-Z. Bao, Y.-H. Peng, H.-Y. Feng, and C.-H. Yang, "Multi-objective aerodynamic optimization design of variable camber leading and trailing edge of airfoil," *Proceedings of the Institution of Mechanical Engineers*, vol. 236, pp. 4748–4765, 2022.

[22] W. Lu, Y. Tian, and P. Liu, "Aerodynamic optimization and mechanism design of flexible variable camber trailing-edge flap," *Chinese Journal of Aeronautics*, vol. 30, no. 3, pp. 988–1003, 2017.

[23] M. Tripathi, M. M., P. Pandey, and R. S. Pant, "Drag mitigation of trilobed airship hull through aerodynamic comparison with conventional single-lobed hull," *Journal of Aerospace Engineering*, vol. 36, no. 6, 2023.

[24] Z.-P. Han, *Exterior Ballistics of Projectiles and Arrows*, Beijing Institute of Technology Press, Beijing, 2014.

[25] H.-T. Li, X.-G. Wang, and Y. Zhao, "Design of two-body separation simulation software considering complex factors," *Journal of System Simulation*, vol. 12, pp. 2851–2859+2866, 2013.

[26] G. H. Ceotto, R. N. Schmitt, G. F. Alves, L. A. Pezente, and B. S. Carmo, "RocketPy: six degree-of-freedom rocket trajectory simulator," *Journal of Aerospace Engineering*, vol. 34, no. 6, 2021.

[27] Z.-Q. Guo, X.-H. Jiang, and Y. Wang, "Numerical study on gas acceleration of afterburning propellant projectiles," *Chinese Journal of High-Pressure Physics*, vol. 26, no. 5, pp. 564–570, 2012.

[28] T. Kray, J. Franke, and W. Frank, "Magnus effect on a rotating sphere at high Reynolds numbers," *Journal of Wind Engineering and Industrial Aerodynamics*, vol. 110, pp. 1–9, 2012.

[29] J. Yin, X. Wu, and J. Lei, "Body-fin interference on the Magnus effect of spinning projectile in supersonic flows," *Engineering Applications of Computational Fluid Mechanics*, vol. 11, no. 1, pp. 496–512, 2017.